



Understanding the complementarities of surface-enhanced infrared and Raman spectroscopies in CO adsorption and electrochemical reduction

Chang, Xiaoxia; Vijay, Sudarshan; Zhao, Yaran; Oliveira, Nicholas J.; Chan, Karen; Xu, Bingjun

Published in:
Nature Communications

Link to article, DOI:
[10.1038/s41467-022-30262-2](https://doi.org/10.1038/s41467-022-30262-2)

Publication date:
2022

Document Version
Publisher's PDF, also known as Version of record

[Link back to DTU Orbit](#)

Citation (APA):
Chang, X., Vijay, S., Zhao, Y., Oliveira, N. J., Chan, K., & Xu, B. (2022). Understanding the complementarities of surface-enhanced infrared and Raman spectroscopies in CO adsorption and electrochemical reduction. *Nature Communications*, 13(1), Article 2656. <https://doi.org/10.1038/s41467-022-30262-2>

General rights

Copyright and moral rights for the publications made accessible in the public portal are retained by the authors and/or other copyright owners and it is a condition of accessing publications that users recognise and abide by the legal requirements associated with these rights.

- Users may download and print one copy of any publication from the public portal for the purpose of private study or research.
- You may not further distribute the material or use it for any profit-making activity or commercial gain
- You may freely distribute the URL identifying the publication in the public portal

If you believe that this document breaches copyright please contact us providing details, and we will remove access to the work immediately and investigate your claim.

Understanding the complementarities of surface-enhanced infrared and Raman spectroscopies in CO adsorption and electrochemical reduction

Xiaoxia Chang^{1,2,3}, Sudarshan Vijay⁴, Yaran Zhao³, Nicholas J. Oliveira³, Karen Chan ⁴✉ & Bingjun Xu ^{1,2,3}✉

In situ/operando surface enhanced infrared and Raman spectroscopies are widely employed in electrocatalysis research to extract mechanistic information and establish structure-activity relations. However, these two spectroscopic techniques are more frequently employed in isolation than in combination, owing to the assumption that they provide largely overlapping information regarding reaction intermediates. Here we show that surface enhanced infrared and Raman spectroscopies tend to probe different subpopulations of adsorbates on weakly adsorbing surfaces while providing similar information on strongly binding surfaces by conducting both techniques on the same electrode surfaces, i.e., platinum, palladium, gold and oxide-derived copper, in tandem. Complementary density functional theory computations confirm that the infrared and Raman intensities do not necessarily track each other when carbon monoxide is adsorbed on different sites, given the lack of scaling between the derivatives of the dipole moment and the polarizability. Through a comparison of adsorbed carbon monoxide and water adsorption energies, we suggest that differences in the infrared vs. Raman responses amongst metal surfaces could stem from the competitive adsorption of water on weak binding metals. We further determined that only copper sites capable of adsorbing carbon monoxide in an atop configuration visible to the surface enhanced infrared spectroscopy are active in the electrochemical carbon monoxide reduction reaction.

¹College of Chemistry and Molecular Engineering, Peking University, Beijing 100871, China. ²Beijing National Laboratory for Molecular Sciences, Beijing 100871, China. ³Center for Catalytic Science and Technology, Department of Chemical and Biomolecular Engineering, University of Delaware, Newark, DE 19716, USA. ⁴CatTheory Center, Department of Physics, Technical University of Denmark, Kongens Lyngby 2800, Denmark. ✉email: kchan@fysik.dtu.dk; b_xu@pku.edu.cn

Electrosynthesis, including the electrochemical CO₂ and CO reduction reactions, referred to as the CO₂RR and the CORR, respectively, has been recognized as a key component in the decarbonization of the energy and chemical sectors with the increasingly affordable and available renewable electricity^{1–3}. A key enabling factor in the development of effective catalytic materials for electrosynthesis is the understanding of how active sites on the catalyst surface facilitate the bond breaking and forming processes in electrochemical transformations⁴. The complexity of electrified solid-liquid interfaces, at which most electrocatalytic transformations occur, renders many ex-situ and non-interfacial specific techniques less effective in providing insights relevant to the reaction conditions⁵. In this regard, surface-enhanced vibrational spectroscopies, including infrared (IR) and Raman, have emerged as potent tools to determine surface compositions^{6–9}, identify reaction intermediates^{10–12}, and elucidate mechanisms^{13–15} for their excellent compatibility with in situ/operando studies.

Surface-enhanced IR and Raman spectroscopies referred to as SEIRAS and SERS, respectively, are complementary techniques in electrocatalytic investigations. It is well established that IR and Raman as molecular spectroscopies provide complementary information, derived from their sensitivity toward the dipole moment and polarizability, respectively, of the substrate. When employed for electrochemical interfacial studies, significant interfacial specificity is required for these techniques, since signals from bulk electrolytes could easily overwhelm the information about the interface. Although the main mechanism for the surface enhancement in SEIRAS and SERS is considered to be similar, i.e., enhanced surface plasma afforded by rough metal surfaces (an electromagnetic mechanism)^{16–19}, several fundamental and practical considerations make these two techniques complementary, more so than their counterparts in molecular spectroscopies.

Firstly, Raman spectroscopy is less sensitive to water than IR spectroscopy, which makes the Kretschmann configuration necessary for SEIRAS. This configuration takes advantage of the attenuated total reflection (ATR) mechanism to avoid excessive absorption of the IR beam in passing through a layer of aqueous electrolyte^{20,21}. The optical property of common ATR crystals, as well as the surface chemistry needed for preparing robust metal films on the surface of the crystal, limits the lower bound of the spectral window in ATR-SEIRAS to ~1000 cm⁻¹. Thus, most M-O (M stands for a metal), M-C, and M-N vibrational modes are outside the spectral window of SEIRAS. Meanwhile, SERS' spectral window could be extended to as low as tens of wavenumbers, enabling it to investigate surface speciation. However, SEIRAS typically possesses better signal-to-noise ratios and higher temporal resolutions within its spectral window than SERS. Secondly, the surface enhancement effect with IR appears less metal-specific than Raman spectroscopy. While Cu, Ag, and Au are the three main SERS active metals, SEIRAS can be conducted on many more metallic surfaces, e.g., Pt, Pd, and Ni¹⁷. The development of the intensity borrowing strategy has extended the applicability of SERS to a wider variety of metal surfaces²². Thirdly, chemical enhancement has been well established in SERS, but documented with SEIRAS. Therefore, there could be varying degrees of discrimination towards surface species depending on these two different techniques.

Despite the aforementioned, well-known complementarities, SEIRAS and SERS have rarely been employed in concert in electrocatalytic studies. SEIRAS has been effective in identifying reaction intermediates in the CO₂RR and CORR^{11,14,23,24}. Surface speciation and reaction mechanisms have been successfully interrogated by SERS in the oxygen evolution and reduction reactions^{12,25}, as well as CO₂RR and CORR^{8,9,26,27}, such as our

in situ observation of oxygen-containing species on Cu surfaces in CORR^{8,9}. The scarcity of studies employing both types of surface-enhanced vibrational spectroscopies could be due to the implicit assumption that, for adsorbed species visible in both techniques, they would yield the same information. This assumption could originate from the well-known fact in molecular vibrational spectroscopies that, if a vibrational mode is both IR and Raman active, its vibrational bands in both spectroscopies will appear at the identical wavenumber. However, this assumption may not hold in the case of SEIRAS and SERS for two main reasons: (1) For an adsorbed species, e.g., CO, on different types of sites, e.g., terrace and defects, in various configurations could have different cross-sections in SEIRAS and SERS. Thus, adsorbates in a certain bonding environment could be discriminated or enhanced with a given technique, and the two techniques could be sampling different subpopulations of an adsorbate. (2) Difference in the chemical enhancement effect with SEIRAS and SERS is expected to introduce additional discrimination/enhancement to certain subpopulations of an adsorbate.

Therefore, there is a clear and urgent need to establish an effective methodology to use SEIRAS and SERS to obtain reliable structure-activity relationships in electrocatalysis. In the limited existing studies with both techniques, Weaver and coworkers reported significant differences in spectra of adsorbed CO on a roughened Au surface²⁸, along with good agreements in spectra of other adsorbed species, e.g., thiocyanide and azide, with SEIRAS and SERS. Such spectral discriminations of certain subpopulations of adsorbates could be induced by changes in (1) dipole moment and polarizability of the vibration normal mode; (2) effectiveness of the electromagnetic enhancement; and (3) effectiveness of the chemical enhancement. The first and third points are inevitably intertwined, as both originate from the electronic structure of the adsorbate and its immediate surroundings. This possibility raises a concerning point for the mechanistic studies of the CO₂RR and CORR, in which adsorbed CO is often the only observable intermediate with vibrational spectroscopies, and its bands are frequently correlated with reactivities^{11,15,29,30}. If only a subpopulation of the adsorbed CO is sampled by SEIRAS or SERS, there is no guarantee that the observed CO with one technique, as well as the corresponding adsorption sites, is responsible for the reaction activity. Thus, a better understanding of the limitation of using a single technique and the complementarity among different techniques in investigating complex electrified interfaces is a prerequisite for developing accurate predictive catalyst design principles for the CORR and beyond.

In this work, we investigated CO adsorption on Pt, Pd, Au and oxide-derived Cu (OD-Cu) surfaces using both SEIRAS and SERS under identical conditions in conjunction with density functional theory (DFT) computations. The same film of each metal was employed in these two spectroscopies to allow for direct comparisons. While CO bands on Pd observed by SEIRAS and SERS at the same conditions are quite consistent with each other in terms of peak position and Stark tuning rate, minor but reproducible differences in spectra from these two techniques are observed on the CO covered Pt surface. Substantial differences appear in SEIRA and SER spectra on relatively weak CO-binding surfaces, i.e., Au and OD-Cu. These observations suggest that the two surface-enhanced vibrational spectroscopies probe different subpopulations of adsorbed CO, e.g., CO adsorbed on surface sites with different local environments. Computational investigations with DFT indicate that CO* on different sites give rise to different IR and Raman intensities, due to differences in the derivatives of the adsorbate dipole moments and polarizabilities. A comparison of CO* and H₂O* binding energies on various metals also suggests that the difference in responses between

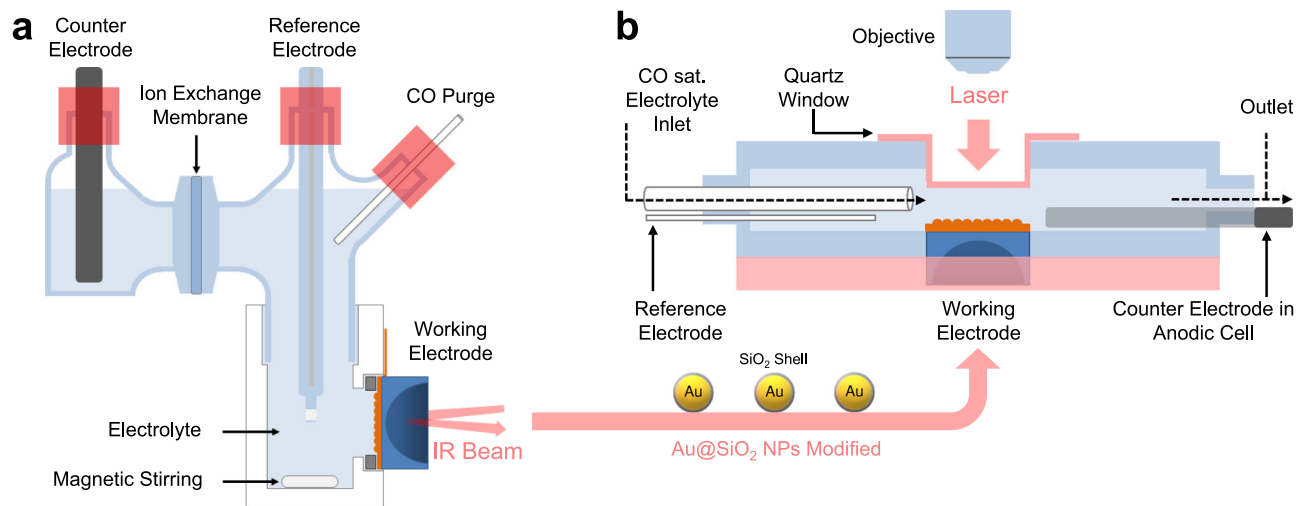


Fig. 1 Schematic of the tandem in situ IR and Raman investigations. **a** Schematic of the spectro-electrochemical cell with stirring function for in situ SEIRAS test. **b** Schematic of the flow cell for in situ SERS test. Both **(a, b)** contain two compartments that are separated by a piece of Nafion membrane.

different surfaces may stem from the competitive adsorption of water, which is more prominent on weak binding metals. Combining SEIRAS, SERS with real-time reactivity tracing, we show that only Cu sites corresponding to CO adsorbed in an atop configuration (CO_{atop}) visible in SEIRAS are active in the CORR.

Results

Tandem tests of in situ SEIRAS and SERS. To enable direct comparisons between SEIRAS and SERS results, we developed an in situ spectroscopic cell and procedures to ensure the same surface was probed by both techniques. SEIRAS tests were conducted on a metal film deposited on a Si ATR crystal fitted in a home-designed spectro-electrochemical cell with a three-electrode configuration (Fig. 1a)³⁰. After the SEIRAS experiment, the Si crystal was removed from the SEIRAS cell, and SiO_2 -coated Au nanoparticles (Au@SiO_2) were introduced onto the film when necessary to enhance the Raman signal²². Au@SiO_2 particles have been shown to be chemically inert in several previous studies^{8,22,31}. The Si crystal was then fitted into a custom-designed three-electrode SERS flow cell (Fig. 1b)^{8,9}. The ability of both SEIRAS and SERS cells to house the Si crystal ensures the two techniques are probing the same surface, and thus results can be directly compared. A reference Si wafer was employed to calibrate the Raman shift by adjusting its lattice peak to 520.7 cm^{-1} before each SERS test. In the following sections, CO is employed as a probe molecule to understand the difference between SEIRAS and SERS on strongly, moderately, and weakly adsorbing surfaces. Then, implications of the complementarity and difference between the two techniques in mechanistic studies are discussed using the CORR on OD-Cu as a model reaction.

Tandem SEIRAS and SERS investigations of CO adsorbed on Pt and Pd surfaces. The affinity of CO to Pt and Pd surfaces and its well-established adsorption behavior make them suitable model systems to compare IR and Raman results^{32–36}. In this work, polycrystalline Pt films were directly deposited on the Si crystal using an electroless chemical plating method, while polycrystalline Pd films were deposited onto a gold substrate layer on the Si crystal through electrodeposition (detailed synthesis methods in Supplementary Information)^{37,38}. The XRD patterns and SEM images of Pt and Pd films show the predominant (111) orientation and rough surface morphology (Supplementary

Fig. 1). The characteristic peaks of Au in the XRD patterns of Pd film originate from its Au substrate (Supplementary Fig. 1c). Both SEIRA and SER spectra on Pt and Pd were collected in CO saturated 0.1 M HClO_4 (pH 1.2).

On Pt, there are minor differences in the adsorbed CO bands between SEIRA and SER spectra. The primary band corresponding to CO adsorbed on the atop position of Pt, i.e., CO_{atop} , was observed in both SEIRA and SER spectra over the entire potential window investigated (0.6 to 0 V vs. reversible hydrogen electrode, or RHE), consistent with previous reports (Fig. 2a and Supplementary Fig. 2)^{39,40}. All potentials reported in this paper are referenced to the RHE scale unless noted otherwise. The CO_{atop} band in both SEIRAS and SERS redshifts as the potential becomes more negative, which is caused by the filling of the antibonding $2\pi^*$ orbital of CO and the vibrational Stark effect^{41,42}. Interestingly, the measured Stark tuning rate is slightly lower with SERS ($21\text{ cm}^{-1}/\text{V}$, green line in Fig. 2b) than with SEIRAS ($29\text{ cm}^{-1}/\text{V}$, blue line in Fig. 2b). The Stark tuning rate determined with SEIRAS in this work is consistent with the previous reports under similar conditions^{40,43,44}. Complementary Pt-C stretching mode was also observed in SER spectrum at lower wavenumbers with expected Stark shifts (Supplementary Fig. 3)⁴⁵. It is worth noting that CO band intensity on Pt in both SEIRAS and SERS changes only slightly (less than 20 and 30%, respectively) in the investigated potential range of 0.6 to 0 V (Supplementary Fig. 2), indicating a negligible impact of CO dynamical dipole coupling on peak shift with the potential. In recent work, we showed that the impact of the coverage effect was less than 8% when the Stark tuning rate was determined using peaks with an integrated area greater than 60% of the maximum value in a given potential range⁴⁶. Thus, the Stark tuning rates of CO on Pt in both SEIRA and SER spectra can be directly determined through the linear fitting of the band wavenumber vs. the applied potential (Fig. 1b). Different Stark tuning rates inevitably lead to different peak positions at different potentials, with the largest difference between SEIRAS and SERS being 4 cm^{-1} at 0 V , which is within the spectral resolution employed in this work (Fig. 2a, b).

The sequence in which SEIRAS and SERS was conducted on the sample did not affect the CO bands, which was confirmed by the reproducible SEIRAS results on the same Pt film after SERS (Supplementary Fig. 2c). Current densities and cyclic voltammetry curves in SEIRAS and SERS tests on Pt are similar (Supplementary Fig. 4), indicating that the difference in the cell

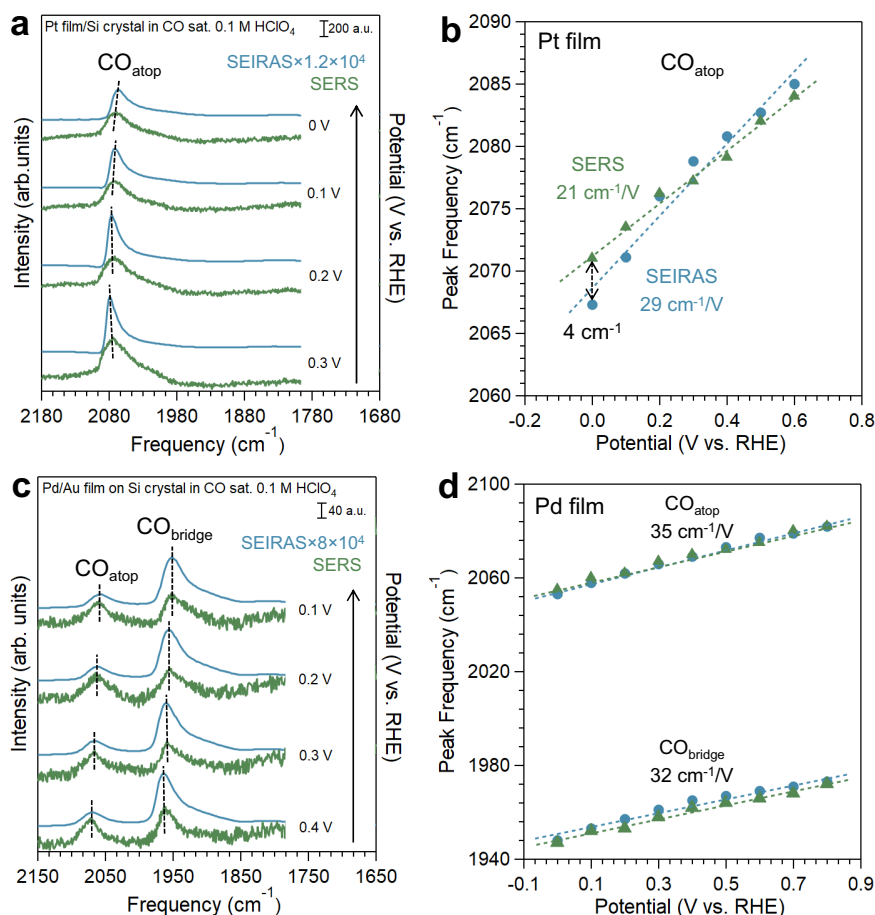


Fig. 2 The comparison between tandem in situ SEIRA (blue) and SER (green) spectra on the same electrode. The spectra on polycrystalline **a** Pt film and **c** Pd film in CO saturated 0.1 M HClO₄ (pH 1.2). The intensity of SEIRA spectra is multiplied by 12,000 and 80,000, respectively, in order to be plotted on the same scale as SER spectra. The dashed lines indicate the difference in peak frequencies between SEIRA and SER spectra under the same potential. The CO peak frequencies in SEIRA (blue circle) and SER (green triangle) spectra on **b** Pt film and **d** Pd film as a function of electrode potential. The Stark tuning rates are labeled.

configuration for these two spectroscopies does not impact the reactivity in any substantial way. Comparable current densities also entail similar interfacial pH, as well as the rates of H⁺ production or consumption. Thus, the different peak positions, and more importantly, Stark tuning rates of the CO_{atop} band observed with SEIRAS and SERS suggest that the adsorbed CO species detected by these two techniques do not overlap entirely. A likely cause is that a subset of adsorbed CO_{atop} in a specific configuration or on a specific type of microenvironment is selectively enhanced by one type of spectroscopy.

Intriguingly, CO bands on Pd observed by SEIRAS and SERS at the same condition are quite consistent with each other. Two sets of bands corresponding to CO adsorbed in the atop and bridge configurations (CO_{atop} and CO_{bridge}, respectively) are present on the Pd surfaces in both SEIRA and SER spectra (Fig. 2c). Both bands redshift as the potential decreases (Supplementary Fig. 5), as expected from the vibrational Stark effect. The peak position shifts of CO_{atop} and CO_{bridge} bands with SEIRAS, 2082–2049 cm⁻¹ and 1973–1940 cm⁻¹, respectively, in the potential window of 0.8 to -0.2 V (Supplementary Fig. 5a) are consistent with previous reports^{47,48}. The most notable feature of CO bands on Pd is that they are remarkably close in SEIRA and SER spectra collected at the same potentials (Fig. 2c and Supplementary Fig. 5), with the difference in peak position less than 3 cm⁻¹. It follows that the Stark tuning rates determined by SEIRAS and SERS are also similar for both

CO_{atop} and CO_{bridge} bands (Fig. 2d). Similar to the case on Pt, CO band intensities in SEIRAS and SERS largely remain constant within the potential range of 0.8 to 0 V (Supplementary Fig. 5), alleviating the need to remove the CO coverage effect on the Stark tuning rate (Fig. 2d). These results suggest that both techniques likely probe the same population of the adsorbed CO. It is important to note that the ratio between the integrated area of CO_{atop} and CO_{bridge} bands is closer to unity in SERS (0.98 at 0 V) than in SEIRAS (0.19 at 0 V, Supplementary Fig. 5). This suggests different enhancement effects of the same adsorbates with different adsorption configurations.

Tandem SEIRAS and SERS investigations of adsorbed CO on Au surface. Au as a well-known weakly adsorbing surface for CO provides another good limiting case in probing the difference between SEIRAS and SERS^{11,35}. A chemically deposited Au film on a Si crystal (Supplementary Fig. 6) was used as the working electrode in CO saturated 0.1 M KHCO₃ (pH 8.9)¹¹. The close to neutral pH of the electrolyte makes chemical erosion of the Au@SiO₂ during the SERS test unlikely. A single CO_{atop} peak centered at 2118–2069 cm⁻¹ appears between 0.8 to 0 V, reaching a maximum peak intensity at ~0.4 to 0.5 V in SEIRAS (Supplementary Fig. 7a, b), similar to the results in a previous report¹¹. Only a CO_{atop} band is observed in SERS (Supplementary Fig. 8a), however, there are three substantial differences in the spectra between these two techniques: (1) The potential window within

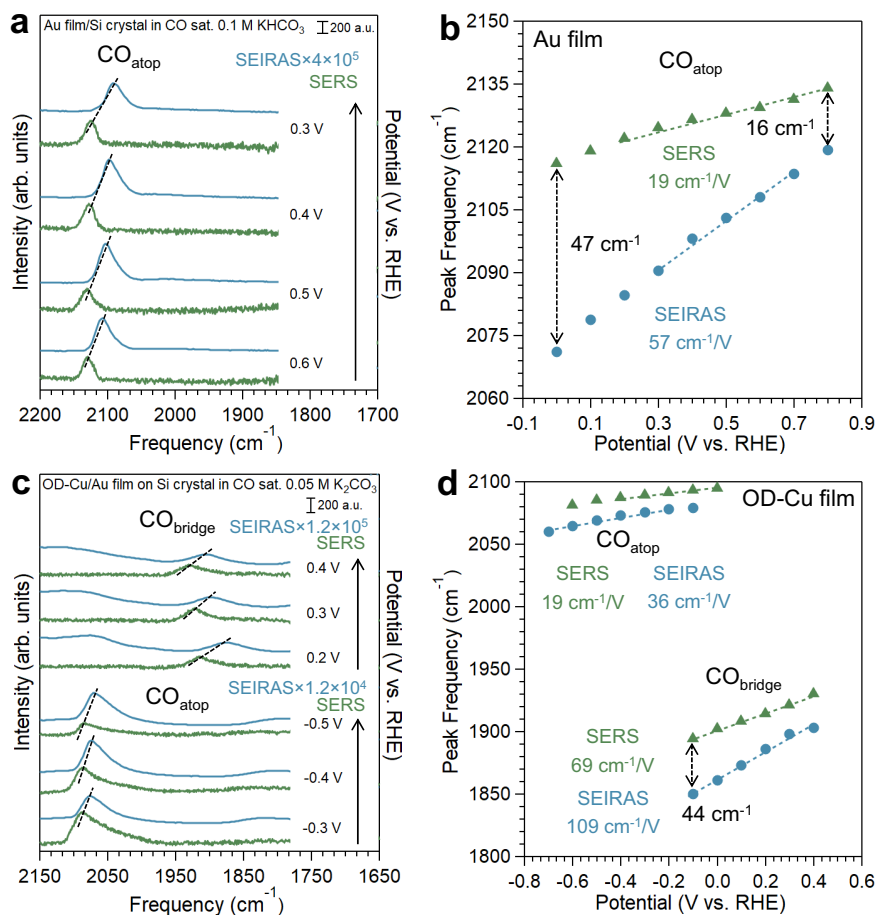


Fig. 3 The comparison between tandem in situ SEIRA (blue) and SER (green) spectra. The spectra on **a** the same polycrystalline Au film and **c** two fresh OD-Cu films in CO saturated 0.1 M KHCO_3 (pH 8.9) and 0.05 M K_2CO_3 (pH 10.6), respectively. The intensity of SEIRAS is scaled up in order to be plotted on the same scale as SERS. The dashed lines indicate the difference in peak frequencies between SEIRA and SER spectra under the same potential. The CO peak frequencies in SEIRA (blue) and SER (green) spectra on **b** Au film and **d** OD-Cu film as a function of electrode potential. The Stark tuning rates are determined by dashed lines and labeled in the figure.

which CO_{atop} appears and the potential at which the CO_{atop} band reaches its maximum are different (Supplementary Figs. 7a, 8a). While the CO_{atop} band becomes barely visible at 0 V with SEIRAS, it reaches its maximum intensity at this potential in SER spectra. (2) Stark tuning rates of the CO_{atop} band are substantially different (Fig. 3b). We found a Stark tuning rate of $19 \text{ cm}^{-1}/\text{V}$ with SERS, and $57 \text{ cm}^{-1}/\text{V}$ with SEIRAS. The CO surface coverage on Au changes substantially with the potential as evidenced by the varying peak area vs. potential in both SEIRAS (Supplementary Fig. 7a, b) and SERS (Supplementary Fig. 8a, b). As a result, the dynamical dipole coupling of CO, i.e., coverage effect, is expected to have a strong impact on the shift of peak position, which complicates the determination of the Stark tuning rate^{49,50}. In order to remove the coverage effect, the Stark tuning rate was determined in the potential ranges of 0.7 to 0.3 V and 0.8 to 0.2 V with SEIRAS and SERS (Fig. 3b and Supplementary Figs. 7c, 8c), respectively, where all peak areas are greater than 60% of the maximum (Supplementary Figs. 7b, 8b) and the impact of coverage effect was less than 8%⁴⁵. (3) The peak position of the CO_{atop} band is consistently lower in SEIRAS than SERS with a maximum difference of 47 cm^{-1} at 0 V, though the difference narrows as the potential increases (Fig. 3a, b). The distinct peak positions and Stark tuning rates of the bands suggest that sub-populations of CO_{atop} in different local environments, e.g., CO adsorbed on terrace versus step sites on different facets, are sampled by the two spectroscopies. It is worth noting that Raman

spectra collected at different spots of the electrode may vary slightly as we reported on Cu microparticles recently⁹. However, variations in peak position among different spots are typically within 10 cm^{-1} and cannot account for the substantial differences (up to 47 cm^{-1}) between IR and Raman spectra (Fig. 3). The magnitude of the difference in the peak positions and Stark tuning rate is larger on Au than Pt, indicating that the discrepancy between the two techniques may correlate with the adsorption strength of CO. As we discuss in the computational section, we postulate that this difference could arise from the competitive adsorption of water on weak binding metals and the resultant change in the distribution of CO as a function of potential.

Tandem SEIRAS and SERS investigations of CO adsorbed on oxide-derived Cu. The ability of Cu to selectively convert CO_2 into valuable multi-carbon products has been a focus of recent research⁵¹. Adsorbed CO is a known intermediate in the electrochemical reduction of CO_2 to multi-carbon products, and the moderate adsorption energy of CO on Cu has been proposed to be a key reason for its ability to facilitate C-C coupling reactions^{35,52,53}. In particular, Cu surfaces after the oxidation-reduction treatment, referred to as oxide-derived Cu or OD-Cu, could significantly reduce the overpotential necessary for multi-carbon products^{54,55}. Thus, OD-Cu is employed in the spectroscopic investigations for CO adsorption, which will be correlated

with reactivity later in this study. OD-Cu films were prepared by the reduction of Cu₂O that was pre-electrodeposited onto the gold substrate layer on a Si crystal¹⁴. The OD-Cu film exhibits a predominant (111) orientation in the XRD pattern (Supplementary Fig. 9a) and roughened morphology as shown by the SEM image (Supplementary Fig. 9b). In contrast to the other metals investigated in this work (Pt, Pd, and Au), which are stable in the potential range investigated even after repeated potential scans, the Cu surface is known to reconstruct at negative potentials, especially in alkaline electrolytes. This instability leads to the varied intensity and lineshape of CO bands depending on the duration the Cu surface has been exposed to the negative potential^{6,9,29,56,57}. Thus, to ensure SEIRA and SER spectra on OD-Cu were collected at comparable conditions, fresh OD-Cu electrodes were employed in SEIRAS and SERS tests, rather than using the same film in the two experiments in tandem. No Au@SiO₂ particles were introduced to the OD-Cu, as this surface is sufficiently rough to enable SERS^{8,9}.

SEIRA and SER spectra were collected during a cathodic potential step from 0.4 to -0.8 V in CO saturated 0.05 M K₂CO₃ (pH 10.6), followed by a reverse anodic scan back to 0.4 V. Both CO_{atop} and CO_{bridge} bands appear in SEIRA and SER spectra, however, in different potential windows and at slightly different wavenumbers. During the initial cathodic potential steps from 0.4 to -0.8 V, a weak CO_{bridge} band at 1903–1778 cm⁻¹ appears in SEIRA spectra with the expected redshift due to the vibrational Stark effect (Supplementary Fig. 10a). Interestingly, no discernable CO_{bridge} band shows up in the SER spectra under otherwise identical conditions (Supplementary Fig. 11a). One possibility is that the lower signal-to-noise ratio, or surface enhancement, of SERS is insufficient to detect such species. We consider this unlikely because a CO_{bridge} band appears in the anodic scan in the SER spectra within the -0.1 to 0.4 V potential window (Fig. 3c and Supplementary Fig. 11a). It stands to reason that if the same bridge-bonded CO species is present in the initial cathodic scan at comparable coverages, the CO_{bridge} band should be detected as well. In contrast, the CO_{bridge} band is quite reversible with SEIRAS (Supplementary Fig. 10a). The peak position and Stark tuning rate of the CO_{bridge} bands in SEIRA and SER spectra during the reverse anodic scan, where the CO_{bridge} band is present in both spectra, do not agree with each other. The CO_{bridge} bands have lower peak positions in SEIRAS than SERS, with a maximum difference of 44 cm⁻¹ at -0.1 V, and SEIRAS shows a larger Stark tuning rate (109 cm⁻¹/V) than SERS (69 cm⁻¹/V) (Fig. 3c, d). The Stark tuning rates of CO_{bridge} bands were directly determined through linearly fitting the band wavenumber vs. the applied potential since the band intensities barely changed with the potential (Supplementary Figs. 10a, 11a). Similar observations were found with the CO_{atop} band, which appears largely at the same potential (~0 V) during the initial cathodic steps (Supplementary Figs. 10a, 11a). The intensity of the CO_{atop} band with SEIRAS peaks at -0.4 V, and the band is highly reversible (Supplementary Fig. 10a, b). In contrast, the CO_{atop} band with SERS reaches its maximum intensity at -0.3 V and does not reappear at the subsequent anodic scan (Supplementary Fig. 11a, b). Different Stark tuning rates of 36 and 19 cm⁻¹/V are determined with SEIRAS and SERS, respectively (Fig. 3d). Similar to the case on Au, we determined the Stark tuning rate of CO_{atop} band on OD-Cu using the peaks with integrated areas greater than 60% of the maximum, i.e., from -0.2 to -0.7 V with SEIRAS and 0 to -0.4 V with SERS (Fig. 3d and Supplementary Figs. 10c, 11c), to remove the coverage effect⁴⁵. Based on these observations, the two spectroscopies are likely probing different subpopulations of both atop- and bridge-bonded CO. Peak positions and Stark tuning rates of CO* by SEIRAS and SERS on different electrodes employed were summarized in Table 1.

Computation of IR and Raman intensities on transition metal surfaces and the impact of competitive water adsorption on potential-dependent vibrational frequencies. To understand the differences in the spectral feature described above, we computed the IR and Raman intensities with DFT calculations for CO* on various sites and facets. The intensities were determined from dipole and polarizability derivatives, respectively, as calculated with a finite-difference grid and the eigenmodes of the dynamical matrix (see Computational Methods). We furthermore determined the CO* and H₂O* binding strengths from published temperature-programmed desorption (TPD) data. In what follows, we discuss the computed Stark tuning rates, the comparison between IR and Raman intensities, and the role of the competitive adsorption of water in the difference in IR and Raman responses with respect to potential in the different metals considered in this work.

Figure 4a–d shows the change in the computed CO* stretch frequency with potential for the top, bridge, and fcc sites on (111) terrace and (211) and (310) steps (see Supplementary Fig. 12 for schematics of the different sites) on Au, Cu, Pd, and Pt. As in the previous studies^{58–62}, we find the frequencies to be within the range 1900–2100 cm⁻¹ for top sites and lower than 1850 cm⁻¹ for bridge and fcc sites. These results are consistent with the theory of CO adsorption on metallic surfaces, which shows the adsorption strength to be determined by the backdonation to the 2π* orbital of adsorbed CO^{42,63}. The higher the coordination number of adsorbed CO has, the weaker the C-O bond is^{64,65}, leading to a lower wavenumber for the C-O stretching mode. Like in the experiments, we determined the Stark tuning rates from the computed potential-dependent CO stretching frequencies as follows:

$$\text{Starktuningrate} = \frac{d\nu}{d(\text{potential})} \quad (1)$$

where ν is the C-O stretch frequency. Figure 4e illustrates the variation of the computed Stark tuning rates against the dipole moments of Au, Cu, Pd, and Pt surfaces. We find that the computed Stark tuning rates are in the range of 0–20 cm⁻¹/V, in line with the previous work^{66,67}, while the experimental values in this work are significantly higher in some cases (up to 100 cm⁻¹/V). The source of this apparently lower computed Stark tuning rate will be discussed below. Stark tuning rates and dipole moments generally track each other, i.e., a larger surface dipole moment of adsorbed CO gives rise to a larger corresponding change in dipole moment with potential. In particular, adsorbed CO on Au has the largest dipole moments (Fig. 4e). There is also a slight variation in the dipoles and corresponding Stark tuning rates on different facets for a particular type of site, but the variations in Stark tuning rate with the type of site tend to have a larger effect, similar to the variations in the CO binding strength.

In general, we find that computed IR and Raman intensities of adsorbed CO do not track each other at any given potential. Figure 4f to i shows the calculated IR and Raman intensities for adsorbed CO on all sites considered in Fig. 4a–d. There is no clear correlation between the IR and Raman intensities at any of the studied potentials (denoted by the color bar), which arises from the general lack of scaling between the derivatives of the dipole moments and polarizabilities. This general lack of scaling holds in the case of individual surface facets (different markers in Fig. 4f–i), though stepped surfaces tend to have comparatively larger IR intensities. This result supports the hypothesis that SEIRAS and SERS can probe different adsorbate subpopulations at a given interface, e.g., CO adsorbed on terrace versus step sites on different facets, and that the difference has its origins in the electronic structure of the adsorbate-metal system.

Table 1 The peak positions and Stark tuning rates of CO* on Pt, Pd, Au, and OD-Cu, respectively.

	Pt	Pd		Au	OD-Cu	
	CO _{atop}	CO _{atop}	CO _{bridge}	CO _{atop}	CO _{atop}	CO _{bridge}
SEIRAS	2084–2067 cm ⁻¹ (0.6 to 0 V) 29 cm ⁻¹ /V	2082–2053 cm ⁻¹ (0.8 to 0 V) 35 cm ⁻¹ /V	1973–1948 cm ⁻¹ (0.8 to 0 V) 32 cm ⁻¹ /V	2114–2090 cm ⁻¹ (0.7 to 0.3 V) 57 cm ⁻¹ /V	2078–2060 cm ⁻¹ (-0.2 to -0.7 V) 36 cm ⁻¹ /V	1850–1903 cm ⁻¹ (-0.1 to 0.4 V) 109 cm ⁻¹ /V
SERS	2084–2071 cm ⁻¹ (0.6 to 0 V) 21 cm ⁻¹ /V	2082–2055 cm ⁻¹ (0.8 to 0 V) 35 cm ⁻¹ /V	1972–1947 cm ⁻¹ (0.8 to 0 V) 32 cm ⁻¹ /V	2134–2122 cm ⁻¹ (0.8 to 0.2 V) 19 cm ⁻¹ /V	2095–2087 cm ⁻¹ (0 to -0.4 V) 19 cm ⁻¹ /V	1894–1930 cm ⁻¹ (-0.1 to 0.4 V) 69 cm ⁻¹ /V

All the potentials are on the RHE scale. The potential ranges in which CO peak intensities are greater than 60% of the maximum are selected to determine the Stark tuning rates.

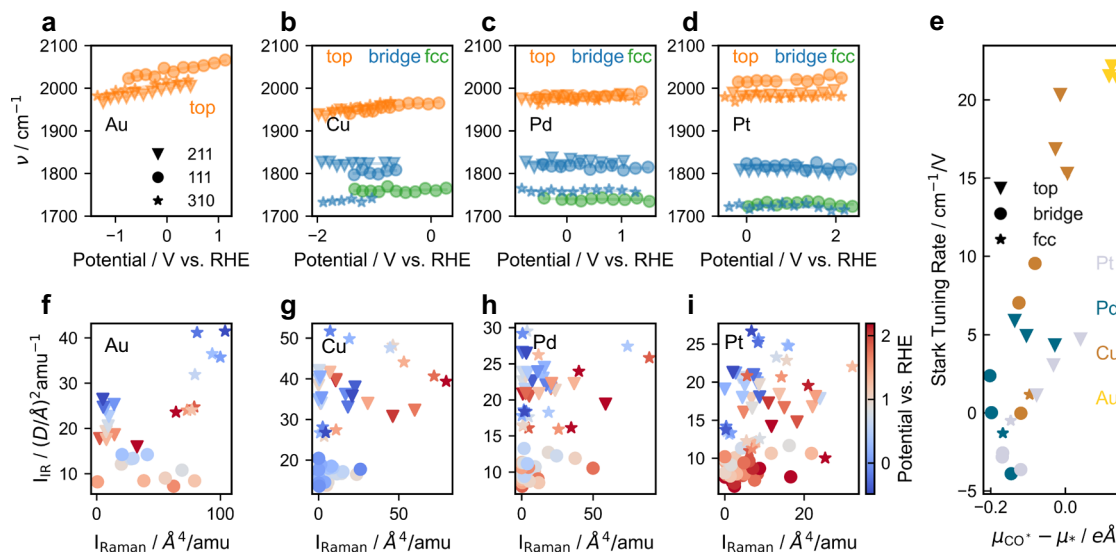


Fig. 4 Computational investigations of CO* on various sites and facets of different metals. DFT-computed vibrational frequencies as a function of the potential for **a** Au, **b** Cu, **c** Pd, and **d** Pt on top, bridge, and fcc sites on the 211, 111, and 310 facets. **e** Surface dipole (x-axis) and Stark tuning rates (y-axis) for all of the studied metals. Scatter plot of IR vs Raman intensities for **f** Au, **g** Cu, **h** Pd, and **i** Pt on facets and sites considered.

We now turn to the experimental observations that Cu and Au have different SERS/SEIRAS responses, while Pt and Pd do not. We suggest that this difference might arise from the degree of competitive water adsorption, which is more prominent in the weak binding metals of Cu and Au. In an aqueous environment, water can potentially compete for surface sites⁶⁸, depending on its affinity to the surface. On weak binding metals like Au, water and CO have similar binding strengths⁶⁹, which leads to their effectively weak adsorption on the surface. Figure 5a highlights this effect by showing the computed Boltzmann CO coverage as a function of different CO and H₂O free energies of adsorption. The Boltzmann coverage of CO is given by the Eq. (2):

$$\theta_{\text{CO}^*} = \frac{\exp\left(-\frac{\Delta G_{\text{CO}}}{k_{\text{B}}T}\right)}{\sum_{i=\text{CO}^*, \text{H}_2\text{O}^*, *}\exp\left(-\frac{\Delta G_i}{k_{\text{B}}T}\right)} \quad (2)$$

When $\Delta G_{\text{CO}} \sim \Delta G_{\text{H}_2\text{O}}$, the Boltzmann coverage of CO is between 1 ML (in red) and no perceptible coverage (in blue). We determined the free energies of adsorbed CO and H₂O of the few representative transition metal facets in Fig. 5a directly from TPD experiments using the methodology in the literature⁷⁰. Briefly, the desorption energies from a TPD curve are fitted to an expression containing the dilute coverage adsorption energy, adsorbate-adsorbate interactions, and the effect of configurational entropy (see Computational Methods). We use energies directly from TPD curves as opposed to DFT calculations in this analysis due to the current inability of static DFT calculations to

accurately predict water adsorption on transition metal surfaces^{71–74}.

In the case of Au(310), both adsorbed CO and H₂O bind weakly ($\Delta G_{\text{CO}} \sim \Delta G_{\text{H}_2\text{O}}$). With comparable binding strengths, their coverages are lowered from what they would be in the absence of the other species. In contrast, on strong binding metals like Pt(111), Ni(111), and Rh(111), ΔG_{CO} is significantly larger than $\Delta G_{\text{H}_2\text{O}}$, and the interfacial water is unlikely to alter the CO coverage. Thus, the coverage of adsorbed CO at a particular site is determined by the relative binding energy of CO and H₂O, i.e., the stronger the CO binding strength against that of H₂O, the more likely that there would be a higher CO* coverage on that site (red region in Fig. 5a). Furthermore, competitive water adsorption could depend on the applied potential, since the water adsorption itself has been shown to depend on potential⁷⁵. Recent ab initio molecular dynamics simulations showed the coverage of water increases from 0 ML to up to 0.5 ML on Pt(111) with an increase in the potential of 2 V, along with a concomitant increase in interfacial water-oriented with the oxygen end down towards the surface⁷⁵. The same effect of decreasing water binding at reducing potentials was also observed on Cu(100)⁷⁶. Meanwhile, we do not expect a significant change in CO binding strength with potential. Previous DFT calculations in the presence of an interfacial field suggest a change in CO binding strength of about 0.1 eV over the 0.5 V range^{69,77}.

We now apply this reasoning to our experiments, which show Au to have a Stark tuning rate of 19 cm⁻¹/V from SERS, and

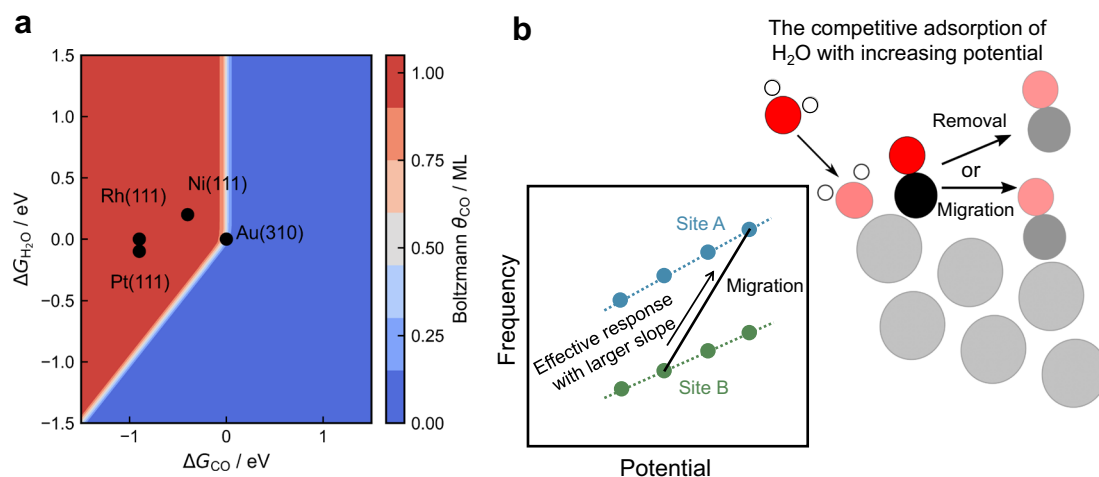


Fig. 5 The competitive adsorption between CO^* and H_2O^* . **a** Boltzmann coverages based on different ΔG_{CO} and $\Delta G_{\text{H}_2\text{O}}$ values with experimental data shown for Au(310)⁹², Pt(111)^{93,94}, Ni(111)^{95,96}, and Rh(111)^{97,98}. **b** Schematics showing the effect of the change in CO^* distribution between Site B (green circles) and Site A (blue circles) on observed vibrational frequencies as a function of potential (left), and cartoon illustrating the effect of competitive H_2O adsorption on CO^* binding site (right). Circles represent different atoms: hydrogen (white), carbon (black), and oxygen (red). The deep and light color shades indicate the molecules at lower and higher potentials, respectively.

$57\text{ cm}^{-1}/\text{V}$ from SEIRAS (Fig. 3b). The computed Stark tuning rates (Fig. 4a) are $\sim 20\text{ cm}^{-1}/\text{V}$ on all sites. Figure 5b (right panel) shows schematically a possible mechanism through which the electrode potential could impact the apparent Stark tuning rate based on our hypothesis. As the potential increases on the Au surface from 0.3 to 0.8 V_{RHE} , water adsorption has been calculated to be more favorable^{75,76,78}, which would give rise to a decreasing CO coverage on steps⁶⁹. Meanwhile, the coverage of CO on terrace sites, which are less affected by water adsorption, is expected to either increase or remain constant based on the calculated adsorption energies of CO^{69,79}. The large apparent Stark tuning rate would result from the gradual shift in the predominance of the signal of adsorbed CO on steps at lower potentials to that of adsorbed CO on terraces at higher potentials (see schematic in Fig. 5b's left panel), as CO adsorbed on terrace sites have a higher wavenumber than those on step sites based on the computational results (Fig. 4a). We note that a larger apparent Stark tuning rate would also appear if the coverage of CO on steps and terraces decreases with the decrease more significant on stepped sites. This effect is more pronounced in the IR than in Raman spectra because the calculated changes in the dipole moment derivative in adsorbed CO are more sensitive to a shift from the highly stepped Au(310) facet to Au(111) than that of the polarizability derivative (such as in Fig. 4f for Au), which qualitatively explains the discrepancy of the measured Stark tuning rates with the two techniques. This effect could also occur on Cu, which binds both CO and water weakly, however, the predominant adsorption sites could also change from the formation of an oxide phase at more anodic potentials. In contrast, in the case of Pt and Pd, coverages on the various sites are unlikely to change due to the dependence of water adsorption strength on potential. CO binds much more strongly than water on these surfaces, which suggests a fixed CO site distribution where the largest IR and Raman intensities dominate.

Correlating spectroscopic and reactivity observations. The contrasting results of the CO^* bands on OD-Cu, Au, and to a lesser extent on Pt, in SEIRA and SER spectra under otherwise identical conditions point to a methodological dilemma in correlating spectroscopic results with reactivity data in electrocatalysis in general and the CORR in particular. Adsorbed CO is

not only a reaction intermediate in the CO_2RR and CORR, but also serves as a probe to identify various types of active Cu sites. The observations that the two surface-enhanced spectroscopies probe different subpopulations of the adsorbed CO raise the inconvenient possibility that CO adsorbed on the true active sites, even if it exists in sufficient coverage, could be overlooked with one or both techniques. To gain reliable structure-activity relations, it is clearly advantageous to employ multiple in situ techniques, e.g., SEIRAS and SERS, to obtain a comprehensive picture of the types of sites present at the reaction conditions, and reduce the likelihood of missing the adsorbed CO (or other probe molecules) on the true active sites. It is equally important to establish direct correlations between reactivity and spectral signatures, which would enable the identification of specific surface sites responsible for the observed reactivity.

One effective way of correlating spectral features with reactivity is to introduce a perturbation with known effects on the reactivity in spectroscopic experiments. Many recent works, including ours, have shown that the removal of forced convection, e.g., stirring, in a batch cell would significantly suppress the CORR by introducing the mass transport limitation of the scantily soluble CO ^{1,52,80}. The overall current density and the Faradaic efficiency for the CORR products drop precipitously when conducting the reaction without stirring in a batch cell in comparison with results obtained with stirring in both 0.05 M K_2CO_3 and 0.1 M KOH (Supplementary Fig. 13). It can be inferred that CO adsorbed on Cu sites active in the CORR would be preferentially consumed when the reaction is limited by the mass transport of CO. Both CO_{atop} and $\text{CO}_{\text{bridge}}$ bands were monitored during the CORR at -0.7 V in 0.05 M K_2CO_3 before and after stopping stirring (Fig. 6). Right after the forced convection was removed, the intensity of the CO_{atop} band with SEIRAS dropped with the overall current and recovered when the stirring resumed (Fig. 6b). Meanwhile, the $\text{CO}_{\text{bridge}}$ band remained largely unchanged throughout this period (Fig. 6a). This is a clear indication that the sites corresponding to the CO_{atop} band are active in the reaction, while those corresponding to the $\text{CO}_{\text{bridge}}$ band are spectators or poisoned, as claimed in several recent publications^{29,81}. The irreversibility of the CO_{atop} band with potential steps in SERS (Supplementary Fig. 11a) suggests that the corresponding sites are unlikely to be the active sites in the CORR at the steady-state due to its structural instability. The possibility of some sites being so active at -0.7 V that adsorbed CO

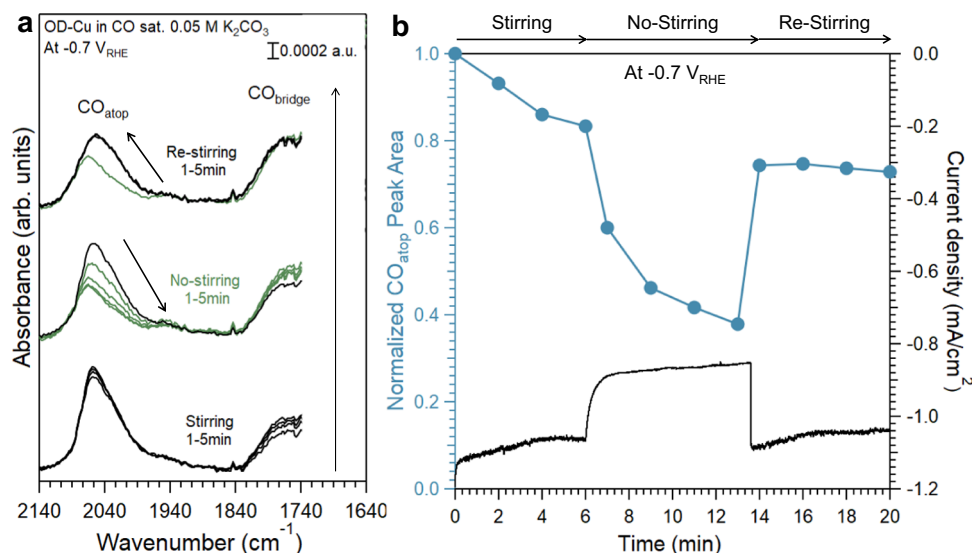


Fig. 6 The impact of stirring on IR spectra and current density. **a** In situ SEIRA spectra on polycrystalline OD-Cu film at -0.7 V in CO saturated 0.05 M K_2CO_3 (pH 10.6) with and without stirring. **b** The normalized peak area of CO_{atop} bands (blue curve) and the current density (black curve) during the SEIRAS test in **a**.

has a residence time too short to be detected by SEIRAS or SERS (unless it is inactive in both spectroscopies) can also be reasonably ruled out. This is because any active sites capable of effectively converting CO are expected to have reasonable adsorption energy of CO, and it follows that such sites should adsorb CO when the potential is insufficiently negative to drive the CORR. No distinct and reversible CO_{atop} band was observed at less negative potentials with SERS, suggesting that such sites do not exist in sufficient coverage to be detected. Thus, the combination of SEIRAS and SERS investigations conclusively shows that only Cu sites on which CO adsorbs in the atop configuration while visible to SEIRAS are responsible for the CORR activity.

Discussion

In summary, CO adsorption on Pt, Pd, Au, and OD-Cu surfaces was investigated in a broad range of electrochemical potentials with in situ surface-enhanced IR and Raman spectroscopies. We demonstrate that the two techniques generally probe different subpopulations of adsorbed CO on metal surfaces, e.g., CO adsorbed on terrace versus step sites on different facets, under identical conditions. The peak position and the Stark tuning rate of CO bands are largely similar on surfaces that bind CO more strongly, such as Pd and Pt, while substantial differences are observed on weakly CO-binding metals, e.g., Au and OD-Cu. Computational investigations suggest that these differences likely originate from the change in the distribution of CO based on the competitive adsorption of water. Combined spectroscopic and reactivity investigations show that only Cu sites corresponding to CO_{atop} band visible in SEIRAS are active in the CORR, while the rest of the Cu sites are either unstable or unable to convert adsorbed CO.

Methods

Polishing and cleaning of Si crystal. Before depositing metal films, Si prisms were thoroughly polished and cleaned. First of all, the Si prisms were immersed in fresh aqua regia solution, which was made with 75% HCl (Fisher Chemical) and 25% HNO_3 (Fisher Chemical), to remove any residual metal species on the surface. Then they were rinsed with deionized water (DI water) and dried with blowing air. Afterward, the Si crystals were polished with a slurry of 0.05 μm Al_2O_3 (Sigma-Aldrich) for several minutes until the surface being hydrophobic. Following that, the Si crystal was sonicated in alternate baths of DI water and acetone three times, to remove alumina powder and any organic residues on the surface. In the end, the Si crystals were dried with blowing air.

Preparation of Pt films on Si crystals. Polycrystalline Pt films were deposited on Si crystals by an electroless chemical plating method^{37,38}. First of all, a Pd seed layer was directly deposited on the reflecting plane of the Si prism in order to improve the adhesion of Pt film⁸². The Pd deposition solution containing 0.23 mM $PdCl_2$ (99.999%, Alfa Aesar), 0.014 M HCl, 0.28 M HF (48%, 99.99% metals basis, Sigma-Aldrich), and 0.76 M NH_4F (40%, Sigma-Aldrich) was prepared in an aqueous solution. Before depositing the Pd seed layer, the Si crystal was first immersed in 40% NH_4F for 1 min and 45 s to make a hydrogen-terminated surface. Then it was immersed in the Pd plating solution at 50 °C for 3 min to obtain the Pd seed layer, after which it was rinsed using DI water, dried with blowing air, and sintered at 200 °C for 30 min in a vacuum evacuated tube furnace. The Pt plating solution consists two separate parts: (1) 0.01 M $H_2PtCl_6 \cdot 6H_2O$ (Sigma-Aldrich) aqueous solution; (2) 0.3 M NH_3 (30%, Fisher Scientific), 0.036 M $HONH_3Cl$ (99.999% Aldrich), and 0.04 M $N_2H_4 \cdot H_2O$ (98%, Sigma-Aldrich). These two solutions were mixed by the volume ratio of 1:1 immediately before Pt deposition. Then the Pd-seeded Si prism was immersed into the mixed Pt plating solution at 60 °C for several minutes, during which a voltmeter was used to check the conductivity of the film until a conductive Pt film was achieved. Then the obtained Pt film was rinsed with DI water and dried with blowing air.

Preparation of Au film on Si crystal. Polycrystalline Au film was deposited onto the Si crystal by chemical bath deposition¹¹. Briefly, the polished Si crystal was first immersed in an NH_4F bath for 120 s to create a hydrogen-terminated surface. The Au plating solution consists of 5.75 mM $NaAuCl_4 \cdot 2H_2O$, 0.025 M NH_4Cl , 0.025 M $Na_2S_2O_3 \cdot 5H_2O$ (98%), 0.075 M Na_2SO_3 (98%), and 0.026 M NaOH (99.99%). All chemicals were purchased from Sigma-Aldrich without further treatment. Before deposition, 0.8 mL of HF aqueous solution (diluted to 2 wt%) was mixed with 4.4 mL above Au plating solution. Then the hydrogen-terminated Si surface was immersed in the above mixture solution for 10 min at 55 °C. After the deposition, the Au film was rinsed using DI water and dried with blowing air.

Preparation of Pd/Au film on Si crystal. Polycrystalline Pd film was electro-deposited onto the obtained Au film on Si crystal⁴³. The Pd plating solution consists of 5 mM $PdCl_2$ and 0.1 M $HClO_4$ (99.999%, Sigma-Aldrich). The electro-deposition was conducted at -200 μA until 100 mC of charge passed through the system, using an Au/Si crystal as the working electrode, a graphite rod as a counter electrode, and a saturated Ag/AgCl (BASi) as the reference electrode. Then the obtained Pd film was rinsed using DI water and dried with blowing air.

Preparation of oxide-derived Cu (OD-Cu)/Au film on Si crystal. OD-Cu film was prepared by electrodepositing Cu_2O onto the obtained Au film on Si crystal and the following electroreduction¹⁴. The electrolytic bath consists of 0.4 M $CuSO_4$ (99.99%, Sigma-Aldrich) and 3 M L-lactic acid ($\geq 85\%$, Sigma-Aldrich). After dissolving the reagents, the pH of this electrolytic bath was adjusted to 11.5 by adding NaOH (99.99%, Sigma-Aldrich) at a constant temperature of 60 °C in a heated water bath. The electro-deposition was carried out potentiostatically under -0.4 V vs. Ag/AgCl using the typical three-electrode system as that in Pd plating process. During the electro-deposition, the water bath was kept under 60 °C and the deposition charge amount was controlled at 100 mC onto the gold substrate layer.

Afterward, the Cu₂O electrode was rinsed using DI water and dried with blowing air. Before the spectroscopic tests, the Cu₂O electrode was pre-reduced through in situ electrochemical reductions in 0.1 M KHCO₃ (prepared by purging CO₂ into K₂CO₃ (99.995%, Sigma-Aldrich) overnight until the pH reached 7.2) under a constant current density of $-500 \mu\text{A}$ until more than 100 mC charge passed and the current density became stable. The obtained OD-Cu film was then rinsed using DI water and dried with blowing air.

Preparation of Au@SiO₂ nanoparticles. The Au@SiO₂ nanoparticles (NPs) were prepared following the method described below³¹. Briefly, Au NPs with an average size of 55 nm were prepared by adding 1.4 mL sodium citrate aqueous solution (1 wt%, 99%, Alfa Aesar) into 200 mL boiling HAuCl₄ aqueous solution (0.01 wt%, 99.99%, Sigma-Aldrich) under vigorous stirring. After that, the mixture was refluxed for 1 h and then cooled to room temperature. Following that, 0.6 mL 1 mM (3-Aminopropyl)triethoxysilane (APTES, 98%, Sigma-Aldrich) solution (pH 11) was added into 30 mL of Au NPs suspension solution and stirred for 15 min at room temperature. Then 3.2 mL sodium silicate solution (0.54 wt%, Sigma-Aldrich) was added to the above mixture and stirred for 5 min. After that, the mixture was kept in a 95 °C oil bath and stirred for another 30 min. The hot solution was then cooled in an ice bath followed by centrifugation at 3400×g and washed with DI water. Finally, the concentrated Au@SiO₂ NPs were dispersed in 500 μL H₂O.

Materials characterization. Scanning electron microscopy (SEM) images were obtained on a field emission scanning electron microscope (ZEISS Auriga 60 SEM/FIB). X-ray diffraction (XRD) spectra were collected on a Bruker D8 Discover diffractometer using a Cu K α X-ray tube.

Preparation of electrolytes. The electrolytes used in this work were all pre-electrolyzed for 24 h at a constant reducing current of -10 mA in a Nafion membrane-separated (IEM, Nafion 211, Fuel Cell Store) two-compartment cell. The Cu foil (99.998%, Sigma-Aldrich) and a graphite rod were employed as working and counter electrodes, respectively. The pre-electrolyzing can deposit most of the metal impurities in the electrolytes onto the Cu foil.

In situ SEIRAS tests. In situ SEIRAS tests were conducted in a home-designed spectro-electrochemical cell with a three-electrode configuration as shown in Fig. 1a. The obtained metal film deposited on Si ATR crystal was used as the working electrode, a graphite rod as the counter electrode, and a saturated Ag/AgCl (BASI) as the reference electrode. The graphite rod was used as the counter electrode in order to avoid any metal contamination⁸³. During the test, CO gas was kept bubbling into the electrolyte and the system was mechanically stirred. The potential on the cell was supplied by a Solartron 1260/1287 system for electrochemical measurements. SEIRA spectra were collected by an Agilent Technologies Cary 660 FTIR spectrometer equipped with a liquid nitrogen-cooled MCT detector. All spectra were collected at a 4 cm^{-1} spectral resolution and presented in absorbance units where a positive and negative peak signifies an increase and decrease in the interfacial species, respectively. All SEIRA spectra presented in this work correspond to 64 coadded scans lasting about 40 s. After the SEIRAS experiment, the working electrode was removed from the SEIRAS cell, rinsed with DI water, and dried with blowing air.

In situ SERS tests. In situ SERS tests were conducted in a custom-designed three-electrode SERS flow cell as shown in Fig. 1b. In this setup, the electrolyte layer between the monochromatic laser and film surface is as thin as 5 mm to avoid the attenuation of scattering light. This flow cell also has two compartments that are separated by a piece of Nafion ion exchange membrane. Before the SERS test, 2 μL of Au@SiO₂ suspension was drop-casted onto the SEIRAS-used films when necessary to enhance the Raman signal. Then the Si crystal was fitted into the SERS flow cell and used as a working electrode, with a graphite rod as the counter electrode in an anodic cell, and a saturated Ag/AgCl (Thomas Scientific) as the reference electrode. SERS tests were performed on a LabRAM HR Evolution microscope (Horiba Jobin Yvon) equipped with a 632.8 nm He-Ne laser, a 50X objective (NA = 0.55), and a monochromator (600 grooves/mm grating), and a CCD detector. The scanning range is 100–2200 cm^{-1} for each SER spectrum, which contains three grating windows, and the acquisition time for each grating window is set to 10 s. Each of the SER spectra presented in this work corresponds to two coadded scans and costs about 80 s. During the test, the fresh electrolyte pre-saturated with CO gas was kept flowing across the cell using an HPLC pump, which can not only replenish CO but also remove H₂ bubbles produced by the hydrogen evolution reaction (HER), thus avoiding the block of scattering light^{8,9}.

Reactivity tests for the electrochemical CO reduction reaction (CORR). The electrochemical reduction of CO on OD-Cu in this work was conducted in the SEIRAS spectrochemical cell shown in Fig. 1a. The OD-Cu film on a copper foil substrate was used as the working electrode, and a graphite rod and a saturated Ag/AgCl were used as the counter and reference electrodes, respectively. Before the reaction, the electrolyte in the cathode compartment was first purged with Ar,

during which the pre-reduction of Cu₂O to OD-Cu was conducted under -0.4 V vs. RHE. The feeding gas was then switched to CO and continuously bubbled into the electrolyte for 0.5 h to reach saturation. Then the cell was sealed, and the reaction was conducted for 10 C of charge under -0.7 V vs. RHE in 0.05 M K₂CO₃ and 0.1 M KOH as shown in Supplementary Fig. 13. After the reaction, the gas products were detected by a GC (Agilent Technologies 7890B) equipped with a Flame Ionization Detector (FID) and Temperature Conductivity Detector (TCD). The liquid products were analyzed by NMR spectroscopy (Bruker AVIII 600) through an integrated peak area ratio with a 4 ppm DMSO/D₂O internal standard.

Computational methods. Density functional theory (DFT) calculations were performed using the GPAW code along with the atomic simulation environment (ASE)^{84–86}. The grid spacing for the real-space grid was set to 0.2 Å and Fermi smearing to 0.1 eV. All calculations were sampled with Monkhorst–Pack *k*-point grids of (4,4,1)⁸⁷. A dipole correction was used in the direction parallel to the surface normal⁸⁸. Continuum charge calculations were done with the solvated jellium model (SJM) implemented within GPAW⁸⁹. The charge was added to the system in increments of 0.2 e from -1 e to $+1 \text{ e}$. A dielectric constant of 78.36 was used. Relaxations were carried out using the Quasi-Newton algorithm implemented within ASE and geometries were converged to forces on all atoms $<0.03 \text{ eV}/\text{Å}^6$. Three surface facets, namely (111), (211), and (310), were investigated for the four metals of Au, Cu, Pd, and Pt. In all cases, we investigated slabs with three metal layers. (3 × 3) surface atoms were used for (111) and (211) and (2 × 3) for (310). The bottom two layers were kept fixed to mimic the bulk metal. On all metals, we considered CO adsorbed on three sites for (111), two sites for (211), and two sites for (310) as shown in Supplementary Fig. 12.

IR and Raman intensities were calculated based on the methodology used in the literature as follows^{87,90}.

1. Vibrational frequencies were computed using the ASE Vibrations class. Eigenmodes (ω) were determined based on the calculated Hessian matrix. A displacement of atoms of 0.01 Å was used throughout.
2. To determine infrared intensities, $I_{\text{IR}} = \left| \frac{d\mu}{dQ} \right|^2$, where μ is the dipole moment and Q is the normal mode (here, for the CO-stretch mode). We computed: (a) the derivative of μ with respect to small displacement R in the x, y, z Cartesian directions as a finite difference, $\frac{d\mu}{dR} = \frac{\mu_x - \mu_{-x}}{2\Delta R}$. (b) The dipole derivative along the normal mode ω was calculated as $\frac{d\mu}{dQ} = \frac{d\mu}{dR} \cdot \omega$.
3. To compute Raman intensities, $I_{\text{Raman}} = \frac{d\alpha}{dR} \cdot \omega$, where α is the polarizability tensor: (a) energies were converged to 10^{-7} eV for each SCF cycle in order to accurately model the polarizability change with displacement (a second derivative quantity). Similar to the literature^{59,90}, we assume that fields in directions perpendicular to the surface normal are small in magnitude so that we consider only the zz component of the polarizability tensor, α_{zz} . We computed this through the second derivative of the forces F with respect to the applied field ξ in the z -direction, $\frac{d\alpha_{zz}}{dR} = \frac{d^2F}{d\xi^2}$, where ξ is applied in the form of a saw-tooth potential. In practice, this quantity was computed using a finite-difference stencil as $\frac{d^2F}{d\xi^2} = \frac{(F_i - 2F_0 - F_{-i})}{d\xi^2}$, where $d\xi = 0.1 \text{ V}/\text{Å}$ and F_i, F_0 , and F_{-i} are the forces corresponding to the different fields.

The adsorption energies of CO* and H₂O* were determined using the methodology detailed in the literature⁷⁰. Briefly temperature-programmed desorption data from experiments were used to determine desorption energy, E_d , which can be fit to the following functional form:

$$E_d = E_0 - b\theta_{\text{sat}}\theta_{\text{rel}} - k_B T \ln \left(\frac{\theta_{\text{rel}}\theta_{\text{sat}}}{1 - \theta_{\text{rel}}\theta_{\text{sat}}} \right)$$

where E_0 is the adsorption energy at dilute coverage, θ_{sat} is the saturation coverage that occurs during dosage, θ_{rel} is the relative coverage which decreases as the temperature is increased and b is a linear adsorbate–adsorbate interaction parameter.

Data availability

Source data are provided with this paper. All relevant data are available from the authors on reasonable request.

Code availability

Scripts used to generate the computational figures can be found at <https://github.com/sudarshav01/ir-raman-co> or in ref. ⁹¹.

Received: 30 November 2021; Accepted: 11 April 2022;

Published online: 12 May 2022

References

1. Nitopi, S. et al. Progress and perspectives of electrochemical CO₂ reduction on copper in aqueous electrolyte. *Chem. Rev.* **119**, 7610–7672 (2019).

2. De Luna, P. et al. What would it take for renewably powered electrosynthesis to displace petrochemical processes? *Science* **364**, eaav3506 (2019).
3. Chang, X., Wang, T. & Gong, J. CO₂ photo-reduction: insights into CO₂ activation and reaction on surfaces of photocatalysts. *Energy Environ. Sci.* **9**, 2177–2196 (2016).
4. Aran-Ais, R. M., Gao, D. & Roldan Cuenya, B. Structure- and electrolyte-sensitivity in CO₂ electroreduction. *Acc. Chem. Res.* **51**, 2906–2917 (2018).
5. Zhu, Y., Wang, J., Chu, H., Chu, Y.-C. & Chen, H. M. In situ/operando studies for designing next-generation electrocatalysts. *ACS Energy Lett.* **5**, 1281–1291 (2020).
6. Gunathunge, C. M. et al. Spectroscopic observation of reversible surface reconstruction of copper electrodes under CO₂ reduction. *J. Phys. Chem. C* **121**, 12337–12344 (2017).
7. Bodappa, N. et al. Early stages of electrochemical oxidation of Cu(111) and polycrystalline Cu surfaces revealed by in situ Raman spectroscopy. *J. Am. Chem. Soc.* **141**, 12192–12196 (2019).
8. Zhao, Y. et al. Speciation of Cu surfaces during the electrochemical CO reduction reaction. *J. Am. Chem. Soc.* **142**, 9735–9743 (2020).
9. Chang, X., Zhao, Y. & Xu, B. pH Dependence of Cu surface speciation in the electrochemical CO reduction reaction. *ACS Catal.* **10**, 13737–13747 (2020).
10. Chen, Y. X., Miki, A., Ye, S., Sakai, H. & Osawa, M. Formate, an active intermediate for direct oxidation of methanol on Pt electrode. *J. Am. Chem. Soc.* **125**, 3680–3681 (2003).
11. Dunwell, M. et al. The central role of bicarbonate in the electrochemical reduction of carbon dioxide on gold. *J. Am. Chem. Soc.* **139**, 3774–3783 (2017).
12. Dong, J.-C. et al. In situ Raman spectroscopic evidence for oxygen reduction reaction intermediates at platinum single-crystal surfaces. *Nat. Energy* **4**, 60–67 (2018).
13. Firet, N. J. & Smith, W. A. Probing the reaction mechanism of CO₂ electroreduction over Ag films via operando infrared spectroscopy. *ACS Catal.* **7**, 606–612 (2016).
14. Chang, X., Malkani, A., Yang, X. & Xu, B. Mechanistic insights into electroreductive C-C coupling between CO and acetaldehyde into multicarbon products. *J. Am. Chem. Soc.* **142**, 2975–2983 (2020).
15. Zhang, H. et al. Computational and experimental demonstrations of one-pot tandem catalysis for electrochemical carbon dioxide reduction to methane. *Nat. Commun.* **10**, 3340 (2019).
16. Linic, S., Christopher, P. & Ingram, D. B. Plasmonic-metal nanostructures for efficient conversion of solar to chemical energy. *Nat. Mater.* **10**, 911–921 (2011).
17. Toporski, J., Hollricher, O. & Dieing, T. *Confocal Raman Microscopy* (Springer, 2018).
18. Lin, K. Q. et al. Plasmonic photoluminescence for recovering native chemical information from surface-enhanced Raman scattering. *Nat. Commun.* **8**, 14891 (2017).
19. Osawa, M. Surface-enhanced infrared absorption. *Top. Appl. Phys.* **81**, 163 (2001).
20. Mojet, B. L., Ebbesen, S. D. & Lefferts, L. Light at the interface: the potential of attenuated total reflection infrared spectroscopy for understanding heterogeneous catalysis in water. *Chem. Soc. Rev.* **39**, 4643–4655 (2010).
21. Kas, R. et al. In-situ infrared spectroscopy applied to the study of the electrocatalytic reduction of CO₂: theory, practice and challenges. *Chemphyschem* **20**, 2904–2925 (2019).
22. Li, J. F. et al. Shell-isolated nanoparticle-enhanced Raman spectroscopy. *Nature* **464**, 392–395 (2010).
23. Zhu, S., Jiang, B., Cai, W. B. & Shao, M. Direct observation on reaction intermediates and the role of bicarbonate anions in CO₂ electrochemical reduction reaction on Cu surfaces. *J. Am. Chem. Soc.* **139**, 15664–15667 (2017).
24. Chou, T. C. et al. Controlling the oxidation state of Cu electrode and reaction intermediates for electrochemical CO₂ reduction to ethylene. *J. Am. Chem. Soc.* **142**, 2857–2867 (2020).
25. Ze, H. et al. Molecular insight of the critical role of Ni in Pt-based nanocatalysts for improving the oxygen reduction reaction probed using an in situ SERS borrowing strategy. *J. Am. Chem. Soc.* **143**, 1318–1322 (2021).
26. Li, F. et al. Molecular tuning of CO₂-to-ethylene conversion. *Nature* **577**, 509–513 (2020).
27. Gao, J. et al. Selective C-C coupling in carbon dioxide electroreduction via efficient spillover of intermediates as supported by operando Raman spectroscopy. *J. Am. Chem. Soc.* **141**, 18704–18714 (2019).
28. Corrigan, D. S., Gao, P., Leung, L. W. H. & Weaver, M. J. Comparisons between surface infrared and surface-enhanced Raman spectroscopies: band frequencies, bandwidths, and selection rules for pseudohalide and related adsorbates at gold and silver electrodes. *Langmuir* **2**, 744–752 (1986).
29. Gunathunge, C. M., Ovalle, V. J., Li, Y., Janik, M. J. & Waagele, M. M. Existence of an electrochemically inert CO population on Cu electrodes in alkaline pH. *ACS Catal.* **8**, 7507–7516 (2018).
30. Malkani, A. S., Dunwell, M. & Xu, B. Operando spectroscopic investigations of copper and oxide-derived copper catalysts for electrochemical CO reduction. *ACS Catal.* **9**, 474–478 (2018).
31. Li, J. F. et al. Surface analysis using shell-isolated nanoparticle-enhanced Raman spectroscopy. *Nat. Protoc.* **8**, 52–65 (2013).
32. Igarashi, H., Fujino, T. & Watanabe, M. Hydrogen electro-oxidation on platinum catalysts in the presence of trace carbon monoxide. *J. Electroanal. Chem.* **391**, 119–123 (1995).
33. Gao, D. et al. Size-dependent electrocatalytic reduction of CO₂ over Pd nanoparticles. *J. Am. Chem. Soc.* **137**, 4288–4291 (2015).
34. Shi, C., Hansen, H. A., Lausche, A. C. & Norskov, J. K. Trends in electrochemical CO₂ reduction activity for open and close-packed metal surfaces. *Phys. Chem. Chem. Phys.* **16**, 4720–4727 (2014).
35. Bagger, A., Ju, W., Varela, A. S., Strasser, P. & Rossmeisl, J. Electrochemical CO₂ reduction: a classification problem. *Chemphyschem* **18**, 3266–3273 (2017).
36. Dunwell, M., Yan, Y. & Xu, B. In-situ infrared spectroscopic investigations of pyridine-mediated CO₂ reduction on Pt electrocatalysts. *ACS Catal.* **7**, 5410–5419 (2017).
37. Miki, A., Ye, S. & Osawa, M. Surface-enhanced IR absorption on platinum nanoparticles: an application to real-time monitoring of electrocatalytic reactions. *Chem. Commun.* **14**, 1500–1501 (2002).
38. Yang, X., Nash, J., Oliveira, N., Yan, Y. & Xu, B. Understanding the pH dependence of underpotential deposited hydrogen on platinum. *Angew. Chem. Int. Ed.* **58**, 17718–17723 (2019).
39. Peng, B., Yan, Y.-G. & Cai, W.-B. Surface-enhanced IR spectroscopy investigation on the electro-oxidation of CO adlayer at a polycrystalline Pt film electrode in Cl⁻-containing HClO₄. *Electrochim. Acta* **55**, 8307–8311 (2010).
40. Dunwell, M., Wang, J., Yan, Y. & Xu, B. Surface enhanced spectroscopic investigations of adsorption of cations on electrochemical interfaces. *Phys. Chem. Chem. Phys.* **19**, 971–975 (2017).
41. Blyholder, G. Molecular orbital view of chemisorbed carbon monoxide. *J. Phys. Chem.* **68**, 2772–2777 (1964).
42. Hammer, B., Morikawa, Y. & Norskov, J. K. CO chemisorption at metal surfaces and overlayers. *Phys. Rev. Lett.* **76**, 2141–2144 (1996).
43. Yan, Y. G. et al. Ubiquitous strategy for probing ATR surface-enhanced infrared absorption at platinum group metal-electrolyte interfaces. *J. Phys. Chem. B* **109**, 7900–7906 (2005).
44. Mason, S. E., Grinberg, I. & Rappe, A. M. First-principles extrapolation method for accurate CO adsorption energies on metal surfaces. *Phys. Rev. B* **69**, 161401 (2004).
45. Su, M. et al. In situ Raman study of CO electrooxidation on Pt(hkl) single-crystal surfaces in acidic solution. *Angew. Chem. Int. Ed.* **59**, 23554–23558 (2020).
46. Chang, X. et al. Determining intrinsic Stark tuning rates of adsorbed CO on copper surfaces. *Catal. Sci. Technol.* **11**, 6825–6831 (2021).
47. Miyake, H., Okada, T., Samjeske, G. & Osawa, M. Formic acid electrooxidation on Pd in acidic solutions studied by surface-enhanced infrared absorption spectroscopy. *Phys. Chem. Chem. Phys.* **10**, 3662–3669 (2008).
48. Hoffmann, F. Infrared reflection-absorption spectroscopy of adsorbed molecules. *Surf. Sci. Rep.* **3**, 107 (1983).
49. Hammaker, R. M., Francis, S. A. & Eischens, R. P. Infrared study of intermolecular interactions for carbon monoxide chemisorbed on platinum. *Spectrochim. Acta* **21**, 1295–1309 (1965).
50. Hollins, P. & Pritchard, J. Infrared studies of chemisorbed layers on single crystals. *Prog. Surf. Sci.* **19**, 275–349 (1985).
51. Meng, Y. et al. Recent advances in electrochemical CO₂ reduction using copper based catalysts. *Acta Phys. -Chim. Sin.* **37**, 2006034 (2021).
52. Wang, L. et al. Electrochemical carbon monoxide reduction on polycrystalline copper: effects of potential, pressure, and pH on selectivity toward multicarbon and oxygenated products. *ACS Catal.* **8**, 7445–7454 (2018).
53. Kuhl, K. P., Cave, E. R., Abram, D. N. & Jaramillo, T. F. New insights into the electrochemical reduction of carbon dioxide on metallic copper surfaces. *Energy Environ. Sci.* **5**, 7050–7059 (2012).
54. Li, C. W. & Kanan, M. W. CO₂ reduction at low overpotential on Cu electrodes resulting from the reduction of thick Cu₂O films. *J. Am. Chem. Soc.* **134**, 7231–7234 (2012).
55. Li, C. W., Ciston, J. & Kanan, M. W. Electroreduction of carbon monoxide to liquid fuel on oxide-derived nanocrystalline copper. *Nature* **508**, 504–507 (2014).
56. Kim, Y.-G., Baricuato, J. H. & Soriaga, M. P. Surface reconstruction of polycrystalline Cu electrodes in aqueous HCO₃ electrolyte at potentials in the early stages of CO₂ reduction. *Electrocatalysis* **9**, 526–530 (2018).
57. Popovic, S. et al. Stability and degradation mechanisms of copper-based catalysts for electrochemical CO₂ reduction. *Angew. Chem. Int. Ed.* **59**, 14736–14746 (2020).
58. Feldt, C. D. et al. CO adsorption on Au(332): combined infrared spectroscopy and density functional theory study. *J. Phys. Chem. C* **123**, 8187–8197 (2018).
59. Fang, Y. et al. Toward a quantitative theoretical method for infrared and Raman spectroscopic studies on single-crystal electrode/liquid interfaces. *Chem. Sci.* **11**, 1425–1430 (2020).

60. Gunasooriya, G. T. K. K. & Saeys, M. CO adsorption on Pt(111): from isolated molecules to ordered high-coverage structures. *ACS Catal.* **8**, 10225–10233 (2018).
61. Yim, W.-L. et al. Universal phenomena of CO adsorption on gold surfaces with low-coordinated sites. *J. Phys. Chem. C* **111**, 445–451 (2007).
62. Dabo, I., Wieckowski, A. & Marzari, N. Vibrational recognition of adsorption sites for CO on platinum and platinum-ruthenium surfaces. *J. Am. Chem. Soc.* **129**, 11045–11052 (2007).
63. Blyholder, G. & Allen, M. C. Infrared spectra and molecular orbital model for carbon monoxide adsorbed on metals. *J. Am. Chem. Soc.* **91**, 3158–3162 (2002).
64. Zhu, W. et al. Monodisperse Au nanoparticles for selective electrocatalytic reduction of CO₂ to CO. *J. Am. Chem. Soc.* **135**, 16833–16836 (2013).
65. Reske, R., Mistry, H., Behafarid, F., Roldan Cuenya, B. & Strasser, P. Particle size effects in the catalytic electroreduction of CO₂ on Cu nanoparticles. *J. Am. Chem. Soc.* **136**, 6978–6986 (2014).
66. Mamatkulov, M. & Filhol, J. S. An ab initio study of electrochemical vs. electromechanical properties: the case of CO adsorbed on a Pt(111) surface. *Phys. Chem. Chem. Phys.* **13**, 7675–7684 (2011).
67. Ringe, S. et al. Understanding cation effects in electrochemical CO₂ reduction. *Energy Environ. Sci.* **12**, 3001–3014 (2019).
68. Chang, X. et al. C-C coupling is unlikely to be the rate-determining step in the formation of C₂⁺ products in the copper-catalyzed electrochemical reduction of CO. *Angew. Chem. Int. Ed.* **61**, e202111167 (2022).
69. Vijay, S. et al. Interaction of CO with gold in an electrochemical environment. *J. Phys. Chem. C* **125**, 17684–17689 (2021).
70. Vijay, S. et al. How to extract adsorption energies, adsorbate–adsorbate interaction parameters and saturation coverages from temperature programmed desorption experiments. *Phys. Chem. Chem. Phys.* **23**, 24396–24402 (2021).
71. Sakong, S. & Gross, A. Water structures on a Pt(111) electrode from ab initio molecular dynamic simulations for a variety of electrochemical conditions. *Phys. Chem. Chem. Phys.* **22**, 10431–10437 (2020).
72. Thurmer, K., Nie, S., Feibelman, P. J. & Bartelt, N. C. Clusters, molecular layers, and 3D crystals of water on Ni(111). *J. Chem. Phys.* **141**, 18C520 (2014).
73. Nie, S., Feibelman, P. J., Bartelt, N. C. & Thurmer, K. Pentagons and heptagons in the first water layer on Pt(111). *Phys. Rev. Lett.* **105**, 026102 (2010).
74. Ogasawara, H. et al. Structure and bonding of water on Pt(111). *Phys. Rev. Lett.* **89**, 276102 (2002).
75. Le, J. B., Fan, Q. Y., Li, J. Q. & Cheng, J. Molecular origin of negative component of Helmholtz capacitance at electrified Pt(111)/water interface. *Sci. Adv.* **6**, eabb1219 (2020).
76. Kristoffersen, H. H. & Chan, K. Towards constant potential modeling of CO-CO coupling at liquid water-Cu(100) interfaces. *J. Catal.* **396**, 251–260 (2021).
77. Resasco, J. et al. Promoter effects of alkali metal cations on the electrochemical reduction of carbon dioxide. *J. Am. Chem. Soc.* **139**, 11277–11287 (2017).
78. Iwasita, T., Xia, X. H., Liess, H. D. & Vielstich, W. Electrocatalysis of organic oxidations: influence of water adsorption on the rate of reaction. *J. Phys. Chem. B* **101**, 7542–7547 (1997).
79. Heenen, H. H., Gauthier, J. A., Kristoffersen, H. H., Ludwig, T. & Chan, K. Solvation at metal/water interfaces: an ab initio molecular dynamics benchmark of common computational approaches. *J. Chem. Phys.* **152**, 144703 (2020).
80. Malkani, A. S., Li, J., Anibal, J., Lu, Q. & Xu, B. Impact of forced convection on spectroscopic observations of the electrochemical CO reduction reaction. *ACS Catal.* **10**, 941–946 (2019).
81. Iijima, G., Inomata, T., Yamaguchi, H., Ito, M. & Masuda, H. The role of a hydroxide layer on Cu electrodes in electrochemical CO₂ reduction. *ACS Catal.* **9**, 6305–6319 (2019).
82. Banerjee, S. Ka. J. A study of immersion processes of activating polished crystalline silicon for autocatalytic electrodeless deposition of palladium and other metals. *J. Electrochem. Soc.* **146**, 580 (1999).
83. Dunwell, M., Yang, X., Yan, Y. & Xu, B. Potential routes and mitigation strategies for contamination in interfacial specific infrared spectroelectrochemical studies. *J. Phys. Chem. C* **122**, 24658–24664 (2018).
84. Mortensen, J. J., Hansen, L. B. & Jacobsen, K. W. Real-space grid implementation of the projector augmented wave method. *Phys. Rev. B* **71**, 035109 (2005).
85. Enkovaara, J. et al. Electronic structure calculations with GPAW: a real-space implementation of the projector augmented-wave method. *J. Phys. Condens. Matter* **22**, 253202 (2010).
86. Hjorth Larsen, A. et al. The atomic simulation environment—a Python library for working with atoms. *J. Phys. Condens. Matter* **29**, 273002 (2017).
87. Monkhorst, H. J. & Pack, J. D. Special points for Brillouin-zone integrations. *Phys. Rev. B* **13**, 5188–5192 (1976).
88. Bengtsson, L. Dipole correction for surface supercell calculations. *Phys. Rev. B* **59**, 12301–12304 (1999).
89. Kastlunger, G., Lindgren, P. & Peterson, A. A. Controlled-potential simulation of elementary electrochemical reactions: proton discharge on metal surfaces. *J. Phys. Chem. C* **122**, 12771–12781 (2018).
90. Zayak, A. T. et al. Chemical Raman enhancement of organic adsorbates on metal surfaces. *Phys. Rev. Lett.* **106**, 083003 (2011).
91. Vijay, S. sudarshanv01/ir-raman-co : v.1.0.0. *Zenodo* <https://doi.org/10.5281/zenodo.6398531> (2022).
92. van Reijzen, M. E., van Spronsen, M. A., Docter, J. C. & Juurlink, L. B. F. CO and H₂O adsorption and reaction on Au(310). *Surf. Sci.* **605**, 1726–1731 (2011).
93. Weibel, M. A., Backstrand, K. M. & Curtiss, T. J. Temperature-programmed desorption studies of the interactions of OD and CO with Pt(111). *Surf. Sci.* **444**, 66–78 (2000).
94. Badan, C., Koper, M. T. M. & Juurlink, L. B. F. How well does Pt(211) represent Pt[n(111) × (100)] surfaces in adsorption/desorption? *J. Phys. Chem. C* **119**, 13551–13560 (2015).
95. Shan, J., Aarts, J. F., Kleyn, A. W. & Juurlink, L. B. The interaction of water with Ni(111) and H/Ni(111) studied by TPD and HREELS. *Phys. Chem. Chem. Phys.* **10**, 2227–2232 (2008).
96. Stevens Miller, A. E., Feigerle, C. S. & Lineberger, W. C. Laser photoelectron spectroscopy of CrH⁻, CoH⁻, and NiH⁻: periodic trends in the electronic structure of the transition-metal hydrides. *J. Chem. Phys.* **87**, 1549–1556 (1987).
97. Crowell, J. E. & Somorjai, G. A. The effect of potassium on the chemisorption of carbon monoxide on the Rh(111) crystal face. *Appl. Surf. Sci.* **19**, 73–91 (1984).
98. Beniya, A., Mukai, K., Yamashita, Y. & Yoshinobu, J. Coverage-dependent sticking probability and desorption kinetics of water molecules on Rh(111). *J. Chem. Phys.* **129**, 016101 (2008).

Acknowledgements

This work is supported by the Beijing National Laboratory for Molecular Sciences, and the National Key R&D Program of China (grant number 2021YFA1501003). X.C., Y.Z., N.J.O., and B.X. also acknowledge the support of the National Science Foundation CAREER Program (Award No. CBET-1651625). S.V. and K.C. acknowledge VSUSTAIN Center 9455. The authors acknowledge computational resources from PRACE (project ID: prpa85) and the Juelich Supercomputing Centre.

Author contributions

X.C. and B.X. conceived the idea and designed experiments in this study. X.C. carried out the in situ SEIRAS, SERS, and electrocatalytic experiments. X.C. and B.X. analyzed the experimental results. S.V. and K.C. conducted the DFT calculations and analyzed the data. Y.Z. synthesized Au@SiO₂ nanoparticles and collected SEM images. N.J.O. synthesized chemically deposited Pt films. X.C., S.V., K.C., and B.X. wrote the manuscript.

Competing interests

The authors declare no competing interests.

Additional information

Supplementary information The online version contains supplementary material available at <https://doi.org/10.1038/s41467-022-30262-2>.

Correspondence and requests for materials should be addressed to Karen Chan or Bingjun Xu.

Peer review information *Nature Communications* thanks Mauricio A Palafox and the other, anonymous, reviewers for their contribution to the peer review of this work. Peer reviewer reports are available.

Reprints and permission information is available at <http://www.nature.com/reprints>

Publisher's note Springer Nature remains neutral with regard to jurisdictional claims in published maps and institutional affiliations.



Open Access This article is licensed under a Creative Commons Attribution 4.0 International License, which permits use, sharing, adaptation, distribution and reproduction in any medium or format, as long as you give appropriate credit to the original author(s) and the source, provide a link to the Creative Commons license, and indicate if changes were made. The images or other third party material in this article are included in the article's Creative Commons license, unless indicated otherwise in a credit line to the material. If material is not included in the article's Creative Commons license and your intended use is not permitted by statutory regulation or exceeds the permitted use, you will need to obtain permission directly from the copyright holder. To view a copy of this license, visit <http://creativecommons.org/licenses/by/4.0/>.

© The Author(s) 2022